Nanoscale Advances

ROYAL SOCIETY OF CHEMISTRY

PAPER

View Article Online
View Journal | View Issue

Cite this: *Nanoscale Adv.*, 2023, **5**, 4852

High-performance flower-like and biocompatible nickel-coated Fe_3O_4@SiO_2 magnetic nanoparticles decorated on a graphene electrocatalyst for the oxygen evolution reaction†

Li Ye,[a] Pengcheng Zhu,[a] Tianxing Wang,[a] Xiaolei Li [b] and Lin Zhuang *[a]

The electrocatalytic oxygen evolution reaction (OER) plays a crucial role in renewable clean energy conversion technologies and has developed into an important direction in the field of advanced energy, becoming the focus of basic research and industrial development. Herein, we report the synthesis and application of flower-like nickel-coated Fe_3O_4@SiO_2 magnetic nanoparticles decorated on a graphene electrocatalyst for the OER that exhibit high efficiency and robust durability. The catalysts were optimized using a rotating ring-disk electrode to test their oxygen evolution properties in 1.0 M KOH solution. Importantly, owing to the high specific surface area and conductivity of C_3N_4 and graphene, the as-synthesized Fe_3O_4@SiO_2@NiO/graphene/C_3N_4 exhibits a small Tafel slope of 40.46 mV dec^{-1}, low overpotential of 288 mV at 10 mA cm^{-2}, and robust OER durability within a prolonged test period of 100 h. The cytotoxicity of Fe_3O_4@SiO_2, Fe_3O_4@SiO_2@NiO, and Fe_3O_4@SiO_2@NiO/graphene/C_3N_4 was evaluated in HeLa and MC3T3-E1 cells, demonstrating that they are efficient and biocompatible catalysts for the OER. Owing to its excellent electrocatalytic efficiency and eco-friendliness, Fe_3O_4@SiO_2@NiO/graphene/C_3N_4 has considerable potential as a new multifunctional composite for large-scale applications in catalysis, biology, medicine, and high-efficiency hydrogen production.

Received 27th March 2023
Accepted 5th July 2023

DOI: 10.1039/d3na00195d

rsc.li/nanoscale-advances

1 Introduction

The large-scale exploitation of traditional energy wastes resources and exhausts non-renewable energy (*e.g.*, coal, oil, gas, chemical energy, minerals, and nuclear fuel). Consequently, there is an increasing drive toward limiting the utilization of such energy. This has stimulated global research on clean and sustainable alternative energy sources. Hydrogen energy is not only environmentally friendly but can also deliver a high level of energy. Water electrolysis is considered an important method for the inexpensive production of hydrogen and is an effective method to meet the current increasing energy demand. As a result, many countries, in particular developed countries such as America, Japan, and many European countries, have intensified the development and utilization of electrocatalysis. Owing to its high energy efficiency, quiet operation, efficient power generation, environmental friendliness, simple maintenance, and many other outstanding advantages, electrocatalysis is universally applicable to water splitting.[1] However, this technique is significantly limited by high electrical energy consumption and consequently, high production costs. The major cause of this high-power consumption is that water electrolysis involves two half-reactions: the hydrogen evolution reaction (HER) and the oxygen evolution reaction (OER), both of which are crucial for the overall efficiency of the process. The significant overpotential originates largely from the OER ($2H_2O \rightarrow O_2 + 4H^+ + 4e^-$) at the anode and the HER ($2H^+ + 2e^- \rightarrow H_2$) at the cathode. Evidently, the OER requires the removal of four protons from the water molecule to form an O–O bond, which involves a multi-electron transfer process with a sluggish kinetic response and very high electric power consumption. This is the key factor restricting the overall efficiency of electrochemical water electrolysis and is the biggest obstacle to the water-splitting field in a wide range of practical applications.[2] Therefore, it is necessary to investigate high-efficiency oxygen evolution catalysts to further advance the practical applicability of this field.[3,4]

Typically, the most active electrocatalysts for the OER are noble metal oxides (*e.g.*, IrO_2 and RuO_2),[5,6] which present high current densities at negligible overpotentials. Nevertheless, despite the very high electrocatalytic efficiencies of iridium and ruthenium, conducting an efficient OER remains a major challenge because of the high price, scarcity, and limited

[a]*School of Physics, Institute for Solar Energy Systems, Guangdong Provincial Key Laboratory of Photovoltaics Technologies, Sun Yat-sen University, Guangzhou 510006, China. E-mail: stszhl@mail.sysu.edu.cn*

[b]*Fels Cancer Institute of Personalized Medicine, Department of Cancer and Cellular Biology, Lewis Katz School of Medicine, Temple University, Philadelphia, PA, USA*

† Electronic supplementary information (ESI) available. See DOI: https://doi.org/10.1039/d3na00195d

reserves of precious metals, which significantly impede their large-scale application. Indeed, the relatively low utilization rate of precious metals is the main limitation of OER catalysts.[7–11] To address this concern, the research and development of low-cost and highly efficient non-precious transition metal OER catalysts are the main topics in current catalyst research.[12,13]

The development of appropriate non-noble metal electrocatalysts with high OER activity in electrolytes could be a promising pathway for lowering the cost of water-splitting devices, thereby making hydrogen production inexpensive and efficient.[14–19] Recently, non-noble transition metal-based catalysts (*e.g.*, Co, Mo, Ni, Mn, and Fe-based catalysts) have become research hotspots and have attracted significant attention as promising candidates in the catalysis industry to replace Ir/Ru-based materials as OER electrocatalysts.[20–24] Among them, Fe- and Ni-based electrocatalysts are well known for their catalytic performance in the OER and have been widely explored owing to their widespread availability, high catalytic activity, and environmental friendliness. Nevertheless, the OER performance of pure metal-based catalysts is still unsatisfactory and requires further improvement.[25,26] Concerning the unsatisfactory results reported for OER catalysts, designing efficient, stable, and highly active catalysts remains a challenge. However, the morphology and structure are also very important for the OER catalytic activity of metal-based catalysts. Thus, to solve this problem and improve the catalytic activity, we designed transition metal (*e.g.*, Ni, Fe, and Co) oxide nanoparticles with OER activity that are loaded on carbon materials. Graphene (Gr) and C_3N_4 were introduced into the reaction system. Hence, the excellent electrochemical activity observed was attributed to the synergistic effect between the different chemical components, a large number of exposed active sites, and the fast mass-transfer process due to the hierarchical pore framework.

In this study, we successfully prepared Fe_3O_4 magnetic nanoparticles (MNPs) through a modified polyol solvothermal method at 200 °C. Subsequently, based on Fe_3O_4 MNPs modified with sodium citrate, core–shell Fe_3O_4@SiO_2 MNPs were prepared using an improved version of the Stöber method to improve the stability and practicality of the Fe_3O_4@SiO_2 MNPs. Fe_3O_4@SiO_2@NiO (FSN)/graphene/C_3N_4 was then synthesized *via* a simple solution-reduction method using a Teflon-lined stainless-steel autoclave. Herein, we report the synthesis of nickel-coated C_3N_4 loaded on a graphene catalyst, which exhibits outstanding performance, high efficiency, and robust durability for the OER. Notably, the as-synthesized samples exhibited a low overpotential of 306 mV at 20 mA cm^{-2}, and robust OER durability within a prolonged test period of 100 h, which equals the OER performance of commercial IrO_2. Importantly, FSN/Gr/C_3N_4 is cheaper than noble metal-based catalysts. Benefiting from a good magnetic performance and special physical stability, the as-prepared samples show good material recyclability and reusability potential and can be widely used in various high-tech fields.[27–33] Moreover, the developed catalyst has potential value in many frontier fields including biological effects, catalysis, and sensors.[34–40] In conclusion, we developed a new, economical, and environmentally friendly material with unique advantages and broad application prospects for a modern society that advocates environmental protection.

2 Experimental

2.1 Materials

Ethylene glycol (EG, ≥99%), ethanol (AR, ≥99.5%), iron(III) chloride ($FeCl_3 \cdot 6H_2O$, AR, 99%), and nickel chloride hexahydrate ($NiCl_2 \cdot 6H_2O$, AR, 98%) were purchased from Aladdin Chemicals, China. Trisodium citrate dihydrate (AR, 99%), anhydrous sodium acetate (AR, ≥99%), melamine (99%), and polyethylene glycol (PEG, average Mn 4000) were purchased from Sigma-Aldrich Chemicals. Ammonia solution ($NH_3 \cdot H_2O$, 28 wt% in H_2O) and tetraethyl orthosilicate (TEOS, reagent grade, 98%) were acquired from Shanghai Macklin Biochemical. Deionized (DI) water, which was used in various processes, was synthesized in our laboratory using a Shenzhen Pure Water No. 1 Water Treatment Technology system. The resistivity of the DI water used in this study was 18.25 mΩ cm^{-1}. The graphene used in the samples was provided by Shanghai Aladdin Biochemical Technology.

2.2 Synthesis of Fe_3O_4, Fe_3O_4@SiO_2, and Fe_3O_4@SiO_2@NiO magnetic nanoparticles and Fe_3O_4@SiO_2@NiO/graphene/C_3N_4 composites

Fe_3O_4 MNPs were synthesized using a modified polyol solvothermal method. In the synthesis process, 0.819 g of $FeCl_3 \cdot 6H_2O$ was dissolved in 10 mL EG with magnetic stirring, at room temperature, to form an orange-yellow solution. Subsequently, 0.318 g sodium citrate was added into 20 mL EG with magnetic stirring in a 50 °C water bath for complete dissolution. Next, 1.5 g sodium acetate anhydrous and 1 mL DI H_2O were rapidly added to the mixture and stirred for 30 min until a homogeneous yellow-brown solution was obtained. After vigorous magnetic stirring for 0.5 h, the solution was transferred to a 50 mL Teflon-lined stainless-steel autoclave and subjected to a high-temperature and pressure reaction at 200 °C, for 10 h, under constant temperature conditions, in an electrically heated drying oven. After the autoclave was cooled to room temperature, the products were washed six times with a mixture of DI water and ethanol to remove all impurities. To prevent the MNPs from being oxidized during the drying process, the cleaned samples were placed in a vacuum drying oven and dried at 40 °C for 48 h. Subsequently, approximately 200 mg of the as-synthesized Fe_3O_4 MNPs were collected for further study.

In this study, Fe_3O_4@SiO_2 MNPs with core–shell structures were prepared using an improved version of the classic Stöber method.[41,42] Notably, TEOS was added twice to ensure the homogeneity of the SiO_2 shell. During the coating process, a mixture of 50 mg Fe_3O_4 MNPs, 6 mL DI water, and 40 mL ethanol was evenly dispersed using ultrasonic oscillation for 10 min. The mixture was then transferred to a 250 mL three-necked round-bottom flask with vigorous mechanical stirring (1000 rpm) in a 50 °C water bath to obtain a better coating of

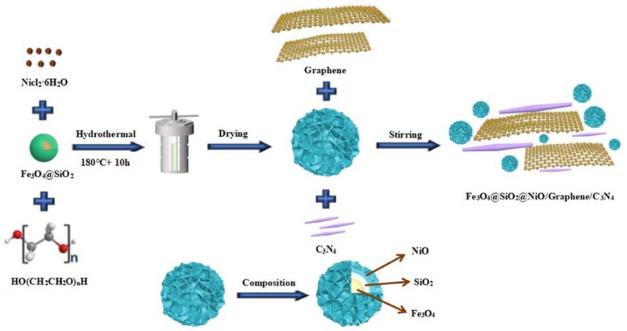

Fig. 1 Formation of the Fe_3O_4@SiO_2@NiO (FSN)/graphene/C_3N_4 composites.

SiO_2. Notably, when wrapping the SiO_2 shell, N_2 was added as a protective gas at the initial stage to ensure that the Fe_3O_4 MNPs were not oxidized by heating. Next, 4 mL concentrated ammonia solution was pipetted into the as-prepared solution and mechanically stirred for 10 min. Subsequently, we used a micropipette to add 120 μL TEOS into the mixture dropwise, in three lots at 30 min intervals, to ensure the uniformity of the SiO_2 shell until the reaction was completed. The products were then collected through magnetic separation, washed six times with ethanol followed by DI water, and finally dried at 40 °C for 48 h in a vacuum. The final product was stored until further use.

For the next synthesis, 100 mg Fe_3O_4@SiO_2 MNPs and 10 mL DI water were mixed and evenly dispersed through ultrasonication. Next, 0.237 g $NiCl_2 \cdot 6H_2O$, 0.1 g PEG, and 0.2 g melamine were added in sequence to 12 mL DI water and stirred for 1 h at 600 rpm using a polytetrafluoroethylene-coated stirrer. Finally, 8 mL H_2O_2 was slowly added to the mixture using a micro-syringe and magnetically stirred for 2 h at 800 rpm, whereby the color of the solution changed from dark to light blue. The aqueous solution was then sealed in a 50 mL Teflon-lined stainless-steel autoclave and maintained at 180 °C for 10 h. After the reaction was completed, the resulting solution was subjected to centrifugal sedimentation at 12 000 rpm for 30 min. The C_3N_4 synthesized with melamine as a carbon source was calcined in an N_2 atmosphere at 550 °C for 2 h. Fig. 1 displays the detailed synthesis process of the FSN/Gr/C_3N_4 composites.

3 Results and discussion

The low-magnification scanning electron microscopy (SEM) images of the FSN MNPs (Fig. 2a and b) show that FSN has a flower-like structure that is assembled by lamellar agglomeration. Fig. S1 (ESI†) displays the SEM images of graphene. In addition, the TEM magnifications of the FSN/Gr/C_3N_4 composites (Fig. 2c, d and S2, ESI†) and FSN MNPs demonstrate that the C_3N_4 and FSN MNPs were successfully decorated on the graphene. Furthermore, in the TEM images (Fig. 2e, f and S3, ESI†), the Fe_3O_4 core, middle silica inner shell, and outermost NiO can be distinguished. In particular, SiO_2 provides the Fe_3O_4@SiO_2 MNPs with good dispersion properties, excellent biocompatibility, good structural stability, and a large surface

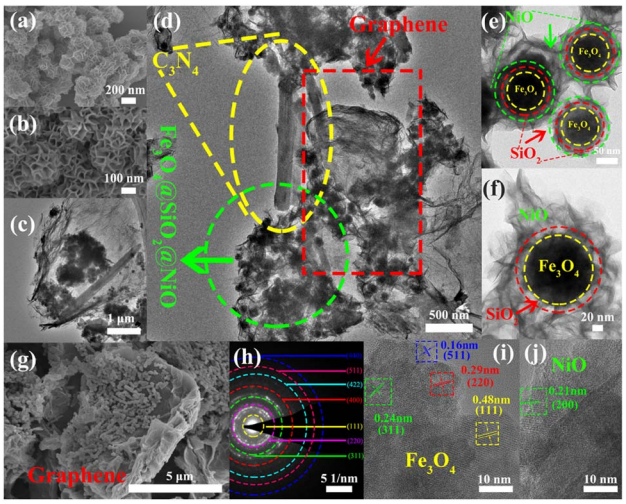

Fig. 2 (a and b) SEM images of the Fe_3O_4@SiO_2@NiO magnetic nanoparticles (FSN MNPs); TEM images of (c and d) FSN/Gr/C_3N_4 and (e and f) FSN MNPs; (g) SEM image of FSN/Gr/C_3N_4; (h) SAED image of the Fe_3O_4 MNPs; (i) HRTEM images of Fe_3O_4; (j) HRTEM images of NiO.

area, properties that are highly desirable for NiO NP coatings. Fig. 2g shows that graphene plays an excellent decorating role in this system, and the FSN nano-chains are well-loaded on the graphene. In Fig. 2h, many brighter diffraction spots within the sharp diffraction rings are observed in the selected area electron diffraction (SAED) pattern, corresponding to the (111), (220), (311), (400), (422), (511), and (440) planes, which indicate the polycrystalline characteristics of the Fe_3O_4 MNPs. Fig. 2i shows the interplanar spacings of 0.16, 0.24, 0.29, and 0.48 nm, which are consistent with the interplanar distances of the (511), (311), (220), and (111) lattice planes in the face-centered cubic (FCC) Fe_3O_4 core, respectively. The high-resolution TEM (HRTEM)

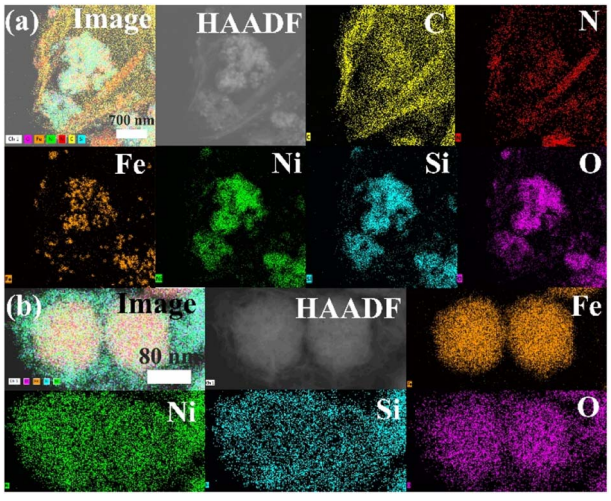

Fig. 3 STEM-HAADF and elemental mapping images of (a) Fe_3O_4@SiO_2@NiO (FSN)/Gr/C_3N_4 and (b) FSN magnetic nanoparticles (MNPs)—elemental Fe (brown), Ni (green), Si (cyan), O (pink), C (yellow), and N (red) mapping.

magnification of NiO shows the (200) plane with an interplanar distance of 0.21 nm in Fig. 2j.

TEM scanning energy-dispersive X-ray spectroscopy (SEDS) was performed to further confirm the composition of FSN/Gr/C_3N_4 (Fig. 3a and b). The elemental Fe (brown), Ni (green), Si (cyan), O (pink), C (yellow), and N (red) mapping of FSN/Gr/C_3N_4 demonstrates the corresponding elemental distributions (Fig. 3a). As shown in Fig. 3b, Fe (brown) is close to the center and is completely covered by the middle shell of Si (cyan), while Ni (green) entirely coats the outermost layer of the surface. These results verify that the FSN MNPs have a uniformly distributed three-layer structure. Therefore, the Fe_3O_4 core, middle dense silica inner shell, and outermost NiO outer shell can be clearly distinguished by comparing the distributions of the different elements.

The surface of the modified Fe_3O_4@SiO_2 MNPs displayed strong electrostatic repulsion and good dispersibility in aqueous solutions, making it a good carrier in drug delivery systems. Indeed, these MNPs can not only be stored for long periods but also maintain a stable structure when constructing biomaterials. The elemental compositions and surface functional groups of FSN and FSN/Gr/C_3N_4 were characterized using high-resolution X-ray photoelectron spectroscopy (HR-XPS; Fig. 4). As shown in the survey spectrum (Fig. 4a), the binding energies at 848.38–870.78, 720.88–731.08, 281.83–292.78, 527.13–537.83, 394.68–404.14, and 98.38–108.38 eV can be attributed to Ni 2p (b), Fe 2p (c), C 1s (d), O 1s (e), Si 2s (f), and N 1s (g) with the corresponding atomic percentages of 13.53, 0.77, 13.15, 53.68, 2.25, and 16.63, respectively. Fig. 4b displays the curve fitting for the Ni $2p_{3/2}$ and Ni $2p_{1/2}$ photoelectron region profiles, which can be observed in two shoulder peaks of (Ni $2p_{3/2}$) and (Ni $2p_{1/2}$) at 856.84 and 874.41 eV, respectively. The energy difference between the Ni $2p_{3/2}$ and $2p_{1/2}$ peaks is approximately 17.5 eV, indicating that the Ni(II) ions in the oxide form have clear symmetry. The peak positions of the Ni $2p_{3/2}$ electron spin orbitals for the FSN MNPs presented in Fig. 4b are located at approximately 856.51 and 857.42 eV. Two other major peaks at approximately 874.01 and 875.26 eV are also observed, which correspond to the characteristic Ni $2p_{1/2}$ orbital. Two significant satellite structures (~862.74 and 880.65 eV) are found on the higher binding energy side of these four peaks. In Fig. 4c, the Fe_{2p} core-level spectrum of the MNPs comprises two binding energy peaks at 712.37 and 723.74 eV assigned to Fe $2p_{3/2}$ and Fe $2p_{1/2}$ peaks, respectively. Fig. 4f clearly shows the XPS spectra of the Si 2s spectrum, which confirms the presence of SiO_2 in the composite and proves that SiO_2 was successfully coated on the surface of Fe_3O_4.

The wide-scan XPS spectrum of the FSN/Gr/C_3N_4 hierarchical structures (Fig. 4h) shows photoelectron lines at binding energies of 98.28–108.08, 279.33–295.33, 394.13–410.53, 526.73–538.58, 720.18–731.68, and 848.98–871.78 eV, which were assigned to Si 2s (m), C 1s (k), N 1s (n), O 1s (l), Fe 2p (j), and Ni 2p (i), respectively. Based on Fig. 4i, the Ni $2p_{1/2}$ (874.57 and 876.03 eV) and Ni $2p_{3/2}$ (857.07 eV and 857.91 eV) peaks correspond to the Ni(II) ions in NiO. In Fig. 4j, the MNP Fe_{2p} spectrum displays two binding energy peaks at approximately 711.96 and 724.84 eV corresponding to Fe $2p_{3/2}$ and Fe $2p_{1/2}$ peaks, respectively, suggesting the presence of Fe_3O_4. Importantly, as shown in Fig. 4n, the N 1s curve can be fitted into two peaks corresponding to N–H (399.25 eV) and C–N (400.67 eV) bonds. The appearance of the C–N bond was due to the addition of C_3N_4 and is markedly different from the bonds shown in Fig. 4g. XPS was also performed to study the surface chemical states of the catalyst before and after the OER.

Compared to the Ni 2p orbital (Fig. S4(a)), Fe 2p orbital (Fig. S4(b)), and O 1s orbital (Fig. S4(c), ESI†) XPS spectra of the catalyst before and after stability, these peaks were almost the same and remain unchanged in location, indicating no surface reconstruction, which also revealed the good chemical state of the catalyst after a 100 h durability test. This means that FSN/Gr/C_3N_4 presents an ultrastable performance for the OER in an alkaline solution, indicating the excellent durability of FSN/Gr/C_3N_4.

To characterize the magnetic properties of Fe_3O_4, Fe_3O_4@SiO_2, FSN, and FSN/Gr/C_3N_4, the magnetic parameters, including the hysteresis loops, saturation magnetization (M_s), retentivity (M_r), and coercivity (H_{ci}), were systematically measured using a vibrating sample magnetometer (VSM) by applying a magnetic field ranging from −30 000 to 30 000 Oe at room temperature (300 K; Fig. 5a). The results revealed that the magnetic saturation strength per unit mass of the sample gradually decreased with the continuous process of modification. With the gradual increase in modifiers, the specific gravity of the modifiers also increased, whereas the Fe_3O_4 content per unit mass of sample powder decreased.[43] When the TEOS content of the sample was

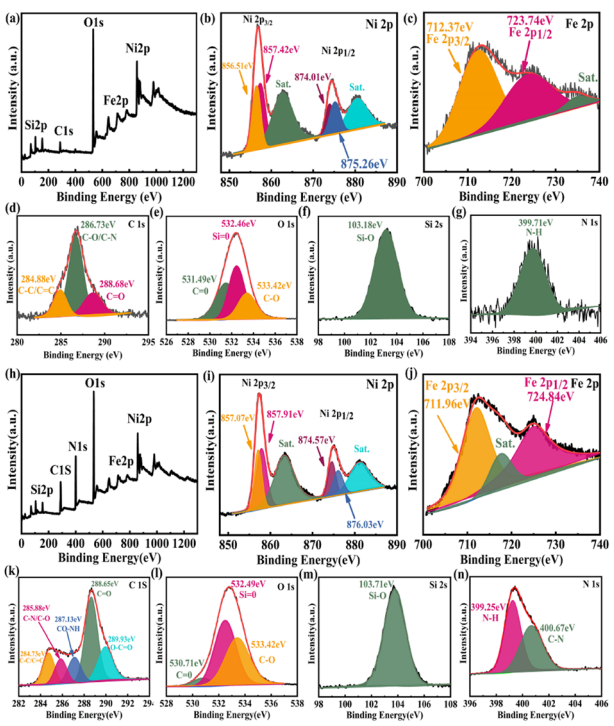

Fig. 4 XPS spectra of the Fe_3O_4@SiO_2@NiO magnetic nanoparticles (FSN MNPs): (a) survey, (b) Ni 2p, (c) Fe 2p, (d) C 1s, (e) O 1s, (f) Si 2s, and (g) N 1s. XPS spectra of the FSN/Gr/C_3N_4 composites: (h) survey, (i) Ni 2p, (j) Fe 2p, (k) C 1s, (l) O 1s, (m) Si 2s, and (n) N 1s.

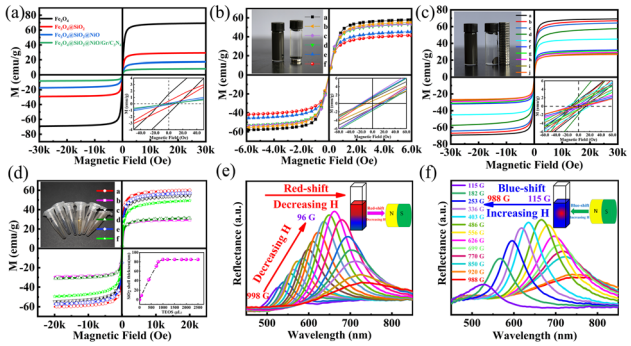

Fig. 5 (a) Hysteresis loops of the Fe_3O_4@SiO_2@NiO magnetic nanoparticles (FSN MNPs) at 300 K (room temperature)—the bottom right of the illustration shows magnified fields at the origin. (b) Hysteresis loops of Fe_3O_4 MNPs with different amounts of sodium acetate at 300 K (a = 2.2, b = 2.0, c = 1.8, d = 1.6, e = 1.5, and f = 1.4 g). (c) Magnetization curves for Fe_3O_4 MNPs using different volumes of DI H_2O: 1, 1.2, 1.4, 1.6, and 1.8 mL—the process of magnetic separation that can be achieved by applying an external magnetic field is illustrated at the top left of the inset. (d) Magnetization loops for core–shell Fe_3O_4 MNPs achieved by using different volumes of TEOS: 0, 120, 180, 240, 360, and 480 μL—the top left of the inset shows the different structural colors of the Fe_3O_4@SiO_2 MNPs. (e and f) Reflection spectra of the Fe_3O_4@SiO_2 MNPs in response to varying magnetic field strength.

0 μL (*i.e.*, Fe_3O_4), the magnetic saturation strength was the highest, reaching 69.23 emu g^{-1}. Because the silica in the Fe_3O_4@SiO_2 MNPs is a nonmagnetic substance, the content of the magnetic substance in the entire particle mass ratio decreased, and the magnetic saturation strength was 29.21 emu g^{-1}. When nickel oxide particles were grown on the surface of the silicon dioxide and when graphene was doped, the measured values were 17.48 and 8.22 emu g^{-1}, respectively. In the region of interaction of the magnetic fields, a weak coercive magnetic field force (13, 8, 5, and 1 Oe) and inappreciable remanence appeared in the four groups of samples near the origin, showing their superparamagnetic nature.

Fig. 5b shows the M–H curve of the Fe_3O_4 MNPs with different amounts of sodium acetate at room temperature corresponding to 57.92, 41.49, 45.29, 53.19, 53.71, and 55.23 emu g^{-1}. The magnetic properties of the samples were measured under cyclic magnetic fields ranging between 6000 and −6000 Oe. The figure clearly shows that the six types of MNPs have a low coercivity force and inappreciable remanence at room temperature and exhibit superparamagnetism characteristics and very high magnetic susceptibility under the action of an external magnetic field. The particle size could be controlled by adjusting the mass ratios of sodium acetate and sodium citrate. In addition, as the relative mass of sodium acetate increased and the size of the Fe_3O_4 MNPs gradually increased, the magnetic saturation also increased, as shown in Fig. 5b. The results in Fig. 5c indicate that the magnetic saturation of the Fe_3O_4 and Fe_3O_4@SiO_2 MNPs changed with the addition of different amounts of DI water, so that the M_s values of Fe_3O_4 MNPs in different volumes of DI H_2O (1, 1.2, 1.4, 1.6, and 1.8 mL) were 69.22, 66.97, 64.29, 57.59, and 44.98 emu g^{-1}, respectively. Furthermore, in the presence of the SiO_2 coating, the corresponding magnetic saturation intensities were 32.07, 31.12, 29.19, 28.03, and 26.71, respectively. When a magnet was placed next to the bottle containing Fe_3O_4 and FSN MNPs dispersed in DI water, the MNPs in the bottle moved rapidly along the direction of the magnetic field and gathered near the magnet, leaving the solution transparent within a few seconds, as displayed in the upper-left insets of Fig. 5b and c. As shown in the lower-right corner of Fig. 5c, these samples exhibited low coercivity and weak remanence, indicating that the Fe_3O_4 core was superparamagnetic. The highest magnetic saturation intensity (60.06 emu g^{-1}) was achieved when the TEOS content of the sample was 0 μL. Notably, there was a negative correlation between the magnetic saturation intensity and the addition of TEOS. Moreover, with the increase in the TEOS content, the magnetic saturation intensity of the samples gradually decreased. Specifically, with increasing added TEOS amounts of 120, 180, 240, 300, 360, and 480 μL, the magnetic saturation intensities of the sample gradually decreased to 60.06, 57.21, 54.62, 49.35, 31.15, and 29.35 emu g^{-1}, respectively. The thickness of SiO_2 could be adjusted by varying the amount of TEOS, and with the increase in the SiO_2 content, the thickness of the core–shell also increased until it plateaued when the amount of TEOS exceeded 1000 μL, as shown in the bottom-right inset of Fig. 5d. When the amount of TEOS was increased continuously, white turbidity was observed in the flask, which was not attached to the surface of Fe_3O_4@SiO_2 and formed SiO_2 spherical pellets. To prevent oxidation of the Fe_3O_4@SiO_2 MNPs during drying, the cleaned samples were dried in a vacuum for 48 h at 40 °C. After drying, Fe_3O_4@SiO_2 MNPs with different structural colors were obtained owing to the different MNP sizes, as shown in the upper-left corner of Fig. 5d. The superparamagnetic properties resulted in a rapid magnetic response, which allowed the Fe_3O_4@SiO_2 MNPs to respond quickly to external magnetic fields. Because of their outstanding magneto-control properties, the reflection spectra of the Fe_3O_4@SiO_2 MNPs for varying magnetic field intensities were also recorded, as shown in Fig. 5e and f. The magnetic field strength slowly decreased from 998 to 96 G, resulting in a red shift in the peak due to the diffraction of the Fe_3O_4@SiO_2 MNPs (Fig. 5e). Similarly, the peak blue-shifted as the magnetic field strength increased from 115 to 998 G (Fig. 5f). The magnetic field, as a new type of external field, has a significant influence on electrocatalytic reactions. Enhancing the efficiency of the OER through magnetic fields has recently received widespread attention as a new regulatory pathway.[44–48]

XRD analysis of the Fe_3O_4, Fe_3O_4@SiO_2, FSN MNPs, and FSN/Gr/C_3N_4 composites was next performed to characterize their structures and phases (Fig. 6a). The seven typical diffraction peaks that appeared from 20° to 70° were assigned to the (111), (220), (311), (400), (422), (511), and (440) planes of iron oxide nanocrystals with an inverse spinel structure, which is consistent with the standard card library (JCPDS No. 19-0629). After the hydrolysis reaction between ammonia, water, and TEOS, no characteristic peaks related to SiO_2 were detected in Fe_3O_4@SiO_2, indicating that SiO_2 was amorphous. Meanwhile, for the FSN and FSN/Gr/C_3N_4 composites, new characteristic XRD diffraction peaks appeared at approximately 37.3°, 43.2°,

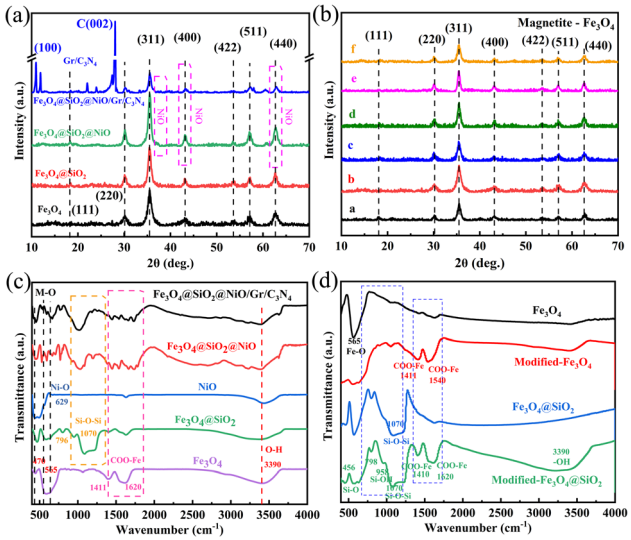

Fig. 6 XRD spectra of (a) Fe_3O_4, Fe_3O_4@SiO_2, and Fe_3O_4@SiO_2@NiO (FSN) magnetic nanoparticles (MNPs) and FSN/Gr/C_3N_4 composites and (b) Fe_3O_4 with different amounts of NaOAc (a = 1.4 g, b = 1.5 g, c = 1.6 g, d = 1.8 g, e = 2.0 g, and f = 2.2 g). FT-IR spectra of (c) Fe_3O_4, Fe_3O_4@SiO_2, NiO, and FSN MNPs and FSN/Gr/C_3N_4 composites and (d) Fe_3O_4, modified-Fe_3O_4, Fe_3O_4@SiO_2 and modified-Fe_3O_4@SiO_2 MNPs.

and 62.9° (Fig. 6a), which correspond to the NiO structure (JCPDS, No. 47-1049). The three additional large and strong characteristic diffraction peaks at approximately 12.85°, 28.11°, and 22.29° correspond to the (100) and (002) planes (JCPDS 87-1526) of C_3N_4 and the (002) planes of graphene, respectively, thereby indicating the successful synthesis of the FSN MNPs and FSN/Gr/C_3N_4 composites.

Fig. 6b clearly shows that for the Fe_3O_4@SiO_2 MNPs with different amounts of anhydrous sodium acetate, there were seven typical diffraction peaks in the six samples: (111), (220), (311), (400), (422), (511), and (440), confirming the crystalline nature of the Fe_3O_4 MNPs. The adjustment effect of sodium acetate and sodium citrate on the size of Fe_3O_4 was due to the interaction of the different forces and hydrolysis rates in the solvothermal process.

The Fourier transform infrared (FTIR) spectrum (Fig. 6c) was used to locate the band positions. Specifically, the strong bands at 629 and 470 cm^{-1} correspond to Ni–O bond vibrations; the strong absorption at 565 cm^{-1} was attributed to the presence of the Fe–O bond in Fe_3O_4; the bonds at approximately 1070, 958, and 456 cm^{-1} were assigned to the Si–O–Si asymmetric stretching vibrations and Si–OH and Si–O bending vibrations, respectively. The FTIR spectra of the Fe_3O_4 MNPs, modified-Fe_3O_4 MNPs, Fe_3O_4@SiO_2 MNPs, and modified Fe_3O_4@SiO_2 MNPs are shown in Fig. 6d. The strong absorption at 565 cm^{-1} was assigned to the Fe–O bond in Fe_3O_4, and this peak confirmed that the product was Fe_3O_4. The bands at approximately 1000–1200, 958, and 456 cm^{-1} were attributed to the Si–O–Si asymmetric stretching vibrations and Si–OH and Si–O bending vibrations, respectively. In the infrared spectrum of Fe_3O_4 modified with sodium citrate, typical COO– absorption peaks were observed at approximately 1540, 1411, 1620, and 1410 cm^{-1}, corresponding to COO– antisymmetric and symmetric vibrations. These results indicated that large amounts of COO– in the sodium citrate strongly bonded with the Fe ions on the surface of the Fe_3O_4 MNPs, forming iron carboxylates. The results also revealed that citrate forms a chemical covalent bond on the surface of Fe_3O_4. Each citric acid group contains three carboxylate groups. When enough citric acid groups are bound to the surface of the Fe_3O_4 MNPs, the strong electrostatic repulsion between the MNPs can overcome the van der Waals force and magnetic dipole interactions, resulting in the stable dispersion of the MNPs in water. The MNPs with a broad and strong absorption band centered at approximately 3390 cm^{-1} were assigned to the O–H stretching vibration on the surface of Fe_3O_4, indicating that under alkaline conditions, citric acid not only cannot completely replace the –OH groups on the surface of Fe_3O_4, but also aids –OH adsorption, which is caused by exposure of some of the citrate carboxyl groups to the solvent. These results are consistent with the XPS results, indicating that Fe_3O_4 was successfully modified.

The OER activity of FSN/Gr/C_3N_4 was investigated by electrochemical measurements at a scan rate of 10 mV s^{-1} in 1.0 M KOH solution. Glassy carbon (GC) was used as the working electrode. Fig. 7a shows the linear sweep voltammetry (LSV) curves of Fe_3O_4@NiO, FSN, FSN/Gr, FSN/Gr/C_3N_4, and IrO_2, which show that the FSN/Gr/C_3N_4 catalyst presented a low overpotential of 288 mV at 10 mA cm^{-2}. Fig. 7b shows the overpotentials of Fe_3O_4@NiO, FSN, FSN/Gr, and FSN/Gr/C_3N_4, and IrO_2 : IrO_2 exhibited an OER onset overpotential of 1.55 V and an overpotential of 350 mV at 10 mA cm^{-2} and a scan rate of 5 mV s^{-1} in 1.0 M KOH solution. Notably, the OER activity of

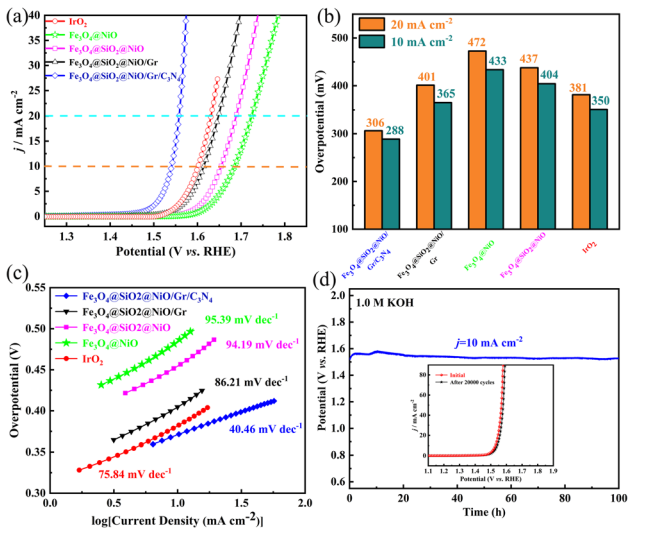

Fig. 7 (a) OER LSV curves of Fe_3O_4, Fe_3O_4@SiO_2, Fe_3O_4@SiO_2@NiO (FSN) MNPs, and FSN/Gr/C_3N_4 composites in O_2-saturated 1.0 M KOH; (b) overpotentials derived from OER polarization curves at j = 10 and 20 mA cm^{-2}; (c) corresponding Tafel plots derived from the OER LSV curves of different catalysts in (a); (d) chronopotentiometric curve for FSN/Gr/C_3N_4 recorded at a constant current density of 10 mA cm^{-2} for 100 h (long-term stability test) in 1.0 M KOH. The inset shows the initial and 20 000th polarization curves of FSN/Gr/C_3N_4.

FSN/Gr/C_3N_4 is superior to that of Fe_3O_4@NiO, FSN, and FSN/Gr and is the same as that of commercial IrO_2 for the overpotential at 10 mA cm^{-2}. Fig. 7c shows Tafel plots obtained by replotting the corresponding OER LSV curves. The Tafel slopes of Fe_3O_4@NiO, FSN, FSN/Gr, FSN/Gr/C_3N_4, and IrO_2 were 94.19, 86.21, 40.46, and 75.84 mV per decade, respectively. As shown in Fig. 7c, the Tafel slope of FSN/Gr/C_3N_4 is considerably lower than those of commercial IrO_2 (75.84 mV per decade) and the other samples. Above all, to evaluate the durability of FSN/Gr/C_3N_4, chronopotentiometry (CP) experiments were performed under a constant current density of 10 mA cm^{-2}. Fig. 7d displays the chronopotentiometry curve of FSN/Gr/C_3N_4 at 10 mA cm^{-2} in 1.0 M KOH with a continuous 100 h test, and the inset demonstrates that the LSV curves of FSN/Gr/C_3N_4 do not change significantly after 20 000 cycles, indicating the excellent durability of FSN/Gr/C_3N_4. As can be seen from Fig. 7d, there is a slight change in the initial potential after the long-term OER test, indicating that the catalyst has excellent electrochemical stability and the activity of the samples can be maintained for 100 h at a constant voltage of about 1.52 V. In sum, FSN/Gr/C_3N_4 exhibits superior OER performance and long-term durability compared to other catalysts. Additionally, the structure and morphology of the catalyst did not change and could also maintain after the long-term OER testing (Fig. S5, ESI†). Fig. S5(a)–(e)† display the SEM images of the FSN/Gr/C_3N_4 catalyst before and after the stability test. Besides, the HRTEM images were further used to rule out the possible interference from the surface reconstruction of catalysts during the OER process. It has been found that the distinctive crystal structure of FSN/Gr/C_3N_4 remained after the electrochemical treatment (Fig. S6, ESI†). Therefore, these results confirm the excellent catalytic activity and structural stability of the FSN/Gr/C_3N_4 catalyst during the OER process.

Moreover, we have also explored the structure–activity relationship between the catalyst and OER performance, and investigated the effects of addition of different components on the catalyst structure and catalytic activity, further discussions and detailed descriptions are indicated in ESI, Section 2.† As illustrated in Fig. S9(a)–(f), ESI,† the decoration of graphene can effectively improve the OER activity of the catalyst, and with the continuous addition of C_3N_4, the catalytic performance of Fe_3O_4@SiO_2@NiO/Gr/C_3N_4 will continue to enhance, ultimately presenting the best catalytic performance.

More importantly, the excellent OER performance of the FSN/Gr/C_3N_4 catalyst is also superior to that of most previously reported catalysts that were tested in similar environments as shown in Table S1 (ESI†), demonstrating that the construction of the Fe_3O_4@SiO_2@NiO/graphene/C_3N_4 composite is a promising strategy to promote the reaction kinetics and reduce the overpotential. For the convenience of comparison, the comparison tables are tabulated in ESI, Table S1.†

All the above results demonstrate that the FSN/Gr/C_3N_4 electrode presents good performance for the OER in 1.0 M KOH, indicating that the catalyst has excellent electrochemical stability during the OER process.

OER kinetics are a multi-electron charge transfer process in an alkaline medium and we consider a four-electron reaction mechanism for the OER. Under alkaline conditions, the water oxidation reaction is given by (eqn (1)):

$$4OH^- \rightarrow O_2(g) + 2H_2O + 4e^- \quad (1)$$

In general, this reaction is usually assumed to proceed in the following four elementary steps and the OER mechanism in an alkaline electrolyte is depicted as follows (eqn (2)–(5)):

$$* + OH^- \rightarrow *OH + e^- \quad (2)$$

$$*OH + OH^- \rightarrow *O + H_2O + e^- \quad (3)$$

$$*O + OH^- \rightarrow *OOH + e^- \quad (4)$$

$$*OOH + OH^- \rightarrow * + O_2 + H_2O + e^- \quad (5)$$

where the * denotes the active site on the catalyst surface. Further discussions and detailed descriptions of the reaction mechanism of the OER are indicated in ESI, Section 1.†

Generally, almost all applications require good biocompatibility and a stable structural basis of the material. To explore the toxic effects of compounds on cells, the detection of cell viability, which includes cell proliferation, is very important in cell culture applications. The interactions between the nanocomposites and mammalian cells were thus evaluated to determine the safety of Fe_3O_4@SiO_2 and FSN/Gr. The CCK-8 assay was used to detect the effects of these samples on the viability of HeLa and MC3T3-E1 cells. HeLa and MC3T3-E1 cells were incubated with different concentrations (0, 0.01, 0.025, 0.05, 0.1, 0.2, 0.3, 0.4, 0.5, 0.6, 0.7, 0.8, 0.9 and 1.0 mg mL^{-1}) of Fe_3O_4@SiO_2, FSN MNPs, and FSN/Gr/C_3N_4 composites. The cytotoxicity of Fe_3O_4@SiO_2, FSN MNPs, and FSN/Gr/C_3N_4 nanocomposites was evaluated in HeLa and MC3T3-E1 cells, as shown in Fig. 8a–d. For the Fe_3O_4@SiO_2 MNPs (Fig. 8a and b), the cell viability did not decrease significantly, and cell proliferation even appeared during the culture process after the

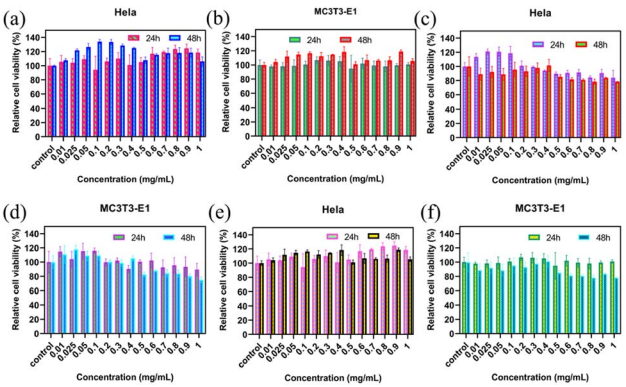

Fig. 8 Cell viability outcomes obtained from CCK-8 assay after 24 and 48 h incubation: HeLa cells and MC3T3-E1 cells are incubated with different concentrations (0, 0.01, 0.025, 0.05, 0.1, 0.2, 0.3, 0.4, 0.5, 0.6, 0.7, 0.8, 0.9, and 1.0 mg mL^{-1}) of (a) and (b) Fe_3O_4@SiO_2 magnetic nanoparticles; (c) and (d) Fe_3O_4@SiO_2@NiO (FSN) MNPs; (e) and (f) FSN/Gr/C_3N_4 composites.

Fe_3O_4@SiO_2 MNPs were added at concentrations of up to 1000 μg mL^{-1} for 24 and 48 h incubation periods. For the FSN MNPs (Fig. 8c and d), cell proliferation was more significant in the early stage, and cell activity decreased slightly when it reached a certain concentration. As shown in Fig. 8e and f, cell proliferation was evident in the HeLa cells, whereas the activity was slightly decreased in the MC3T3-E1 cells. These observed changes in the cell viability of HeLa and MC3T3-E1 cells after co-culture with the samples for 24 and 48 h verify that the Fe_3O_4@SiO_2 MNPs and FSN/Gr/C_3N_4 composites are biocompatible and can be explored for bioimaging inside living cells in the future. Therefore, FSN/Gr/C_3N_4 has excellent biocompatibility, and its biological applications should be further explored.

Fig. 9 and 10 show the laser scanning confocal microscopy images of live/dead staining (100×) when HeLa cells were co-cultured with the FSN/Gr/C_3N_4 composites for 24 and 48 h at different concentrations. The presence of dense living cells (green) and a very small number of dead cells (red) clearly indicates that there were a large number of active cells and almost no dead cells in the co-cultures. These cell viability results show that the prepared FSN/Gr/C_3N_4 composites had almost no adverse effects on the cells and were biocompatible with both human and animal cells, indicating that these FSN/Gr/C_3N_4 composites are promising biocompatible materials for drug delivery, which can also be widely applied in bioelectrocatalysis, electrochemical biosensors, *etc.* Bioelectrocatalysis is an interdisciplinary research field combining biocatalysis and electrocatalysis, which synergistically couples the merits of both biocatalysis and electrocatalysis and provides access to sustainable and highly efficient technological applications.[49–53]

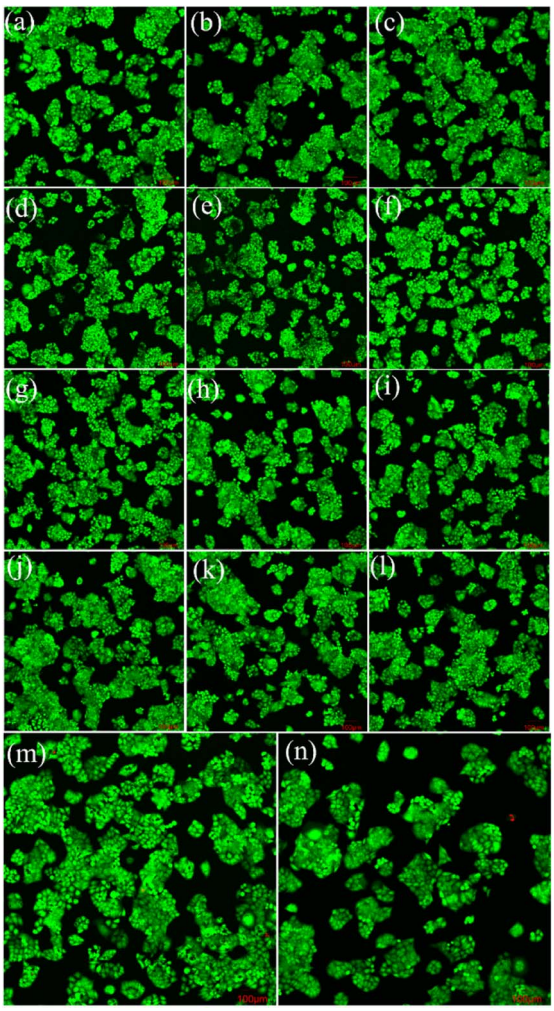

Fig. 9 Laser scanning confocal microscopy images of live/dead staining (100×) for HeLa cells co-cultured with different concentrations of Fe_3O_4@SiO_2@NiO (FSN)/Gr/C_3N_4 composites for 24 h (a = 0, b = 0.01, c = 0.025, d = 0.05, e = 0.1, f = 0.2, g = 0.3, h = 0.4, i = 0.5, j = 0.6, k = 0.7, l = 0.8, m = 0.9, and n = 1.0 mg mL^{-1}).

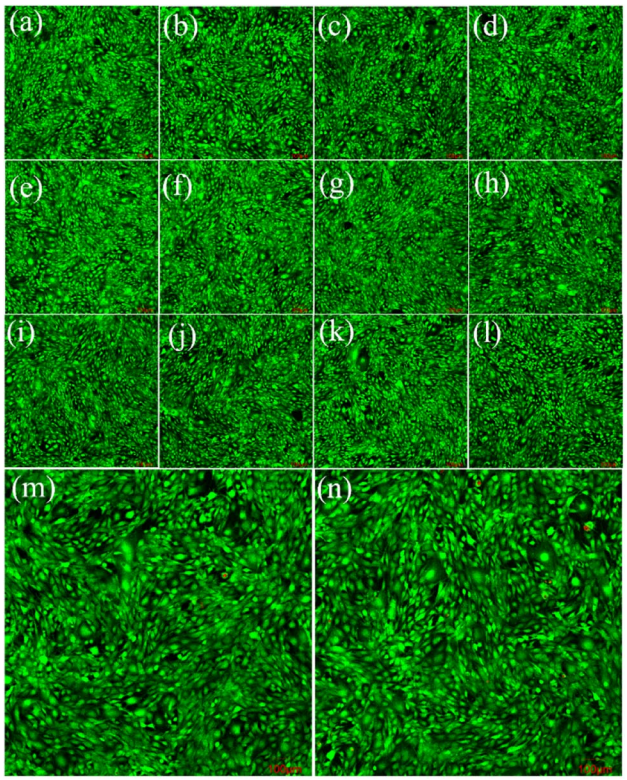

Fig. 10 Laser scanning confocal microscopy images of live/dead staining (100×) for MC3T3-E1 cells co-cultured with different concentrations of Fe_3O_4@SiO_2@NiO (FSN)/Gr/C_3N_4 composites for 24 h (a = 0, b = 0.01, c = 0.025, d = 0.05, e = 0.1, f = 0.2, g = 0.3, h = 0.4, i = 0.5, j = 0.6, k = 0.7, l = 0.8, m = 0.9, and n = 1.0 mg mL^{-1}).

4 Conclusions

In this study, we successfully synthesized superparamagnetic Fe_3O_4 magnetic nanoparticles using a novel solvothermal method and modified them with a citrate group with excellent water dispersity. Fe_3O_4@NiO, Fe_3O_4@SiO_2, and Fe_3O_4@SiO_2@NiO/graphene catalysts were subsequently synthesized using these Fe_3O_4 magnetic nanoparticles. We then developed a graphene substrate by loading Fe_3O_4@SiO_2@NiO magnetic nanoparticles with C_3N_4. The Fe_3O_4@SiO_2@NiO/graphene/C_3N_4

composite exhibited better electrocatalytic performance than the other catalysts in a 1.0 M KOH solution for the OER, which matched that of commercial IrO_2. This excellent catalyst is reported herein for the first time. Owing to the porous multilayer structure of graphene and the high specific surface area of C_3N_4, the Fe_3O_4@SiO_2@NiO/graphene/C_3N_4 composite demonstrates a low overpotential (288 mV), small Tafel slope (40.46 mV per decade), and robust OER durability within a prolonged test period of 100 h. More importantly, the Fe_3O_4@SiO_2@NiO/graphene/C_3N_4 catalyst is easier to prepare than other non-noble metal catalysts and significantly cheaper than commercial IrO_2. This work provides a feasible approach to achieve the strong combination of carbon materials and metal oxides for excellent OER performance. In conclusion, its economy and convenience make our developed composite highly valuable in many bio-related fields.

Author contributions

Lin Zhuang conceived the idea, supervised the project and presented the project outline, guided the whole experiment, and provided funding support. Li Ye conducted the experiments and performed data analysis and writing – original draft. Pengcheng Zhu gave some advice for the characterization and analysis. All the authors discussed the results, commented on the manuscript, and contributed to the final polishing of the manuscript.

Conflicts of interest

There are no conflicts to declare.

Acknowledgements

This work was supported by the National Key R&D Program of China under grants (no. 2021YFA1400900, 2021YFA0718300, and 2021YFA1402100), National Natural Science Foundation of China under grants (no. 61835013, 12174461, and 12234012), and Space Application System of China Manned Space Program. Ms Yao Zhong and Mr Dingyu Song are acknowledged for providing fruitful discussions and a final review of the manuscript.

Notes and references

1 P. Abril, M. P. del Río, C. Tejel, T. W. G. M. Verhoeven, J. W. H. Niemantsverdriet, C. J. M. Van der Ham, K. G. Kottrup and D. G. H. Hetterscheid, Detangling Catalyst Modification Reactions from the Oxygen Evolution Reaction by Online Mass Spectrometry, *ACS Catal.*, 2016, **6**(11), 7872–7875.

2 L. Zhao, X. J. Qin, G. J. Shao and N. Wang, The Influence of H_2O Content in Solvents {Water + Carbinol} and {Water + Ethanol} on the Deposition Mechanism of AZO Films Synthesized by Cold-wall AACVD, *Chem. Vap. Deposition*, 2012, **18**(7–9), 256–262.

3 S. Sun and S. Liang, Recent advances in functional mesoporous graphitic carbon nitride (mpg-C_3N_4) polymers, *Nanoscale*, 2017, **9**(30), 10544–10578.

4 X. Yin, L. Yang and Q. Gao, Core-shell nanostructured electrocatalysts for water splitting, *Nanoscale*, 2020, **12**(30), 15944–15969.

5 O. Diaz-Morales, I. Ledezma-Yanez, M. T. M. Koper and F. Calle-Vallejo, Guidelines for the Rational Design of Ni-Based Double Hydroxide Electrocatalysts for the Oxygen Evolution Reaction, *ACS Catal.*, 2015, **5**(9), 5380–5387.

6 L. Wang, C. Lin, D. Huang, F. Zhang, M. Wang and J. Jin, A comparative study of composition and morphology effect of $Ni_xCo_{1-x}(OH)_2$ on oxygen evolution/reduction reaction, *ACS Appl. Mater. Interfaces*, 2014, **6**(13), 10172–10180.

7 J. Guo, T. Li, Q. Wang, N. Zhang, Y. Cheng and Z. Xiang, Superior oxygen electrocatalysts derived from predesigned covalent organic polymers for zinc-air flow batteries, *Nanoscale*, 2018, **11**(1), 211–218.

8 L. Wang, Y. Huang, X. Sun, H. Huang, P. Liu, M. Zong and Y. Wang, Synthesis and microwave absorption enhancement of graphene@Fe_3O_4@SiO_2@NiO nanosheet hierarchical structures, *Nanoscale*, 2014, **6**(6), 3157–3164.

9 N. J. S. Costa, R. F. Jardim, S. H. Masunaga, D. Zanchet, R. Landers and L. M. Rossi, Direct Access to Oxidation-Resistant Nickel Catalysts through an Organometallic Precursor, *ACS Catal.*, 2012, **2**(6), 925–929.

10 L. Tan, X. Zhang, Q. Liu, J. Wang, Y. Sun, X. Jing, J. Liu, D. Song and L. Liu, Preparation of magnetic core-shell iron oxide@silica@nickel-ethylene glycol microspheres for highly efficient sorption of uranium(VI), *Dalton Trans.*, 2015, **44**(15), 6909–6917.

11 G. Yan, T. Wahler, R. Schuster, M. Schwarz, C. Hohner, K. Werner, J. Libuda and P. Sautet, Water on Oxide Surfaces: A Triaqua Surface Coordination Complex on Co_3O_4(111), *J. Am. Chem. Soc.*, 2019, **141**(14), 5623–5627.

12 J. Jiang, S. Lu, H. Gao, X. Zhang and H.-Q. Yu, Ternary $FeNiS_2$ ultrathin nanosheets as an electrocatalyst for both oxygen evolution and reduction reactions, *Nano Energy*, 2016, **27**, 526–534.

13 S. Li, Y. Wang, S. Peng, L. Zhang, A. M. Al-Enizi, H. Zhang, X. Sun and G. Zheng, Co-Ni-Based Nanotubes/Nanosheets as Efficient Water Splitting Electrocatalysts, *Adv. Energy Mater.*, 2016, **6**(3), 1501661.

14 H. Schäfer, S. M. Beladi-Mousavi, L. Walder, J. Wollschläger, O. Kuschel, S. Ichilmann, S. Sadaf, M. Steinhart, K. Küpper and L. Schneider, Surface Oxidation of Stainless Steel: Oxygen Evolution Electrocatalysts with High Catalytic Activity, *ACS Catal.*, 2015, **5**(4), 2671–2680.

15 L. Wang, J. Geng, W. Wang, C. Yuan, L. Kuai and B. Geng, Facile synthesis of Fe/Ni bimetallic oxide solid-solution nanoparticles with superior electrocatalytic activity for oxygen evolution reaction, *Nano Res.*, 2015, **8**(12), 3815–3822.

16 Z. Zhang, Y. Qin, M. Dou, J. Ji and F. Wang, One-step conversion from Ni/Fe polyphthalocyanine to N-doped carbon supported Ni-Fe nanoparticles for highly efficient water splitting, *Nano Energy*, 2016, **30**, 426–433.

17 Y. Jin, H. Wang, J. Li, X. Yue, Y. Han, P. K. Shen and Y. Cui, Porous MoO_2 Nanosheets as Non-noble Bifunctional Electrocatalysts for Overall Water Splitting, *Adv. Mater.*, 2016, **28**(19), 3785–3790.

18 Y. Xu, B. Chen, J. Nie and G. Ma, Reactive template-induced core-shell FeCo@C microspheres as multifunctional electrocatalysts for rechargeable zinc-air batteries, *Nanoscale*, 2018, **10**(36), 17021–17029.

19 J. Huang, J. Han, R. Wang, Y. Zhang, X. Wang, X. Zhang, Z. Zhang, Y. Zhang, B. Song and S. Jin, Improving Electrocatalysts for Oxygen Evolution Using $Ni_xFe_{3-x}O_4$/Ni Hybrid Nanostructures Formed by Solvothermal Synthesis, *ACS Energy Lett.*, 2018, **3**(7), 1698–1707.

20 Q. Li, L. Wu, G. Wu, D. Su, H. Lv, S. Zhang, W. Zhu, A. Casimir, H. Zhu, A. Mendoza-Garcia and S. Sun, New approach to fully ordered fct-FePt nanoparticles for much enhanced electrocatalysis in acid, *Nano Lett.*, 2015, **15**(4), 2468–2473.

21 I. G. McKendry, L. J. Mohamad, A. C. Thenuwara, T. Marshall, E. Borguet, D. R. Strongin and M. J. Zdilla, Synergistic In-Layer Cobalt Doping and Interlayer Iron Intercalation into Layered MnO_2 Produces an Efficient Water Oxidation Electrocatalyst, *ACS Energy Lett.*, 2018, **3**(9), 2280–2285.

22 X. Wang, H. Xiao, A. Li, Z. Li, S. Liu, Q. Zhang, Y. Gong, L. Zheng, Y. Zhu, C. Chen, D. Wang, Q. Peng, L. Gu, X. Han, J. Li and Y. Li, Constructing NiCo/Fe_3O_4 Heteroparticles within MOF-74 for Efficient Oxygen Evolution Reactions, *J. Am. Chem. Soc.*, 2018, **140**(45), 15336–15341.

23 Y. Zhou, Y. Wu, P. Zhang, J. Chen, B. Qu and J. T. Li, Co_3O_4@(Fe-Doped)$Co(OH)_2$ Microfibers: Facile Synthesis, Oriented-Assembly, Formation Mechanism, and High Electrocatalytic Activity, *ACS Appl. Mater. Interfaces*, 2017, **9**(36), 30880–30890.

24 C. Gadiyar, A. Loiudice, F. D'Ambra, E. Oveisi, D. Stoian, P. Iyengar, L. Castilla-Amoros, V. M antella and R. Buonsanti, Nanocrystals as Precursors in Solid-State Reactions for Size- and Shape-Controlled Polyelemental Nanomaterials, *J. Am. Chem. Soc.*, 2020, **142**(37), 15931–15940.

25 X. Hu, T. Huang, Y. Tang, G. Fu and J. M. Lee, Three-Dimensional Graphene-Supported Ni_3Fe/Co_9S_8 Composites: Rational Design and Active for Oxygen Reversible Electrocatalysis, *ACS Appl. Mater. Interfaces*, 2019, **11**(4), 4028–4036.

26 Q. Zhang, X. Yang and J. Guan, Applications of Magnetic Nanomaterials in Heterogeneous Catalysis, *ACS Appl. Nano Mater.*, 2019, **2**(8), 4681–4697.

27 H. Wang, W. Wang, M. Gui, M. Asif, Z. Wang, Y. Yu, J. Xiao and H. Liu, Uniform Fe_3O_4/Nitrogen-Doped Mesoporous Carbon Spheres Derived from Ferric Citrate-Bonded Melamine Resin as an Efficient Synergistic Catalyst for Oxygen Reduction, *ACS Appl. Mater. Interfaces*, 2017, **9**(1), 335–344.

28 Y. Liang, J. D. Oettinger, P. Zhang and B. Xu, Ni or FeO nanocrystal-integrated hollow (solid) N-doped carbon nanospheres: preparation, characterization and electrochemical properties, *Nanoscale*, 2020, **12**(28), 15157–15168.

29 Y. Jeon, J. Lee, M. Kim, J. Oh, T. Hwang and Y. Piao, Fe_3O_4 nanoparticle decorated three-dimensional porous carbon/MoS_2 composites as anodes for high performance lithium-ion batteries, *Nanoscale*, 2019, **11**(11), 4837–4845.

30 G. Liu, R. Yao, Y. Zhao, M. Wang, N. Li, Y. Li, X. Bo, J. Li and C. Zhao, Encapsulation of Ni/Fe_3O_4 heterostructures inside onion-like N-doped carbon nanorods enables synergistic electrocatalysis for water oxidation, *Nanoscale*, 2018, **10**(8), 3997–4003.

31 S. Sekharan, K. Katayama, H. Kandori and K. Morokuma, Color vision: "OH-site" rule for seeing red and green, *J. Am. Chem. Soc.*, 2012, **134**(25), 10706–10712.

32 Q. Liu, X. Zhang, B. Zhang, Y. Luo, G. Cui, F. Xie and X. Sun, Ambient N_2 fixation to NH_3 electrocatalyzed by a spinel Fe_3O_4 nanorod, *Nanoscale*, 2018, **10**(30), 14386–14389.

33 H. Wang, S. Li, Y. Si, Z. Sun, S. Li and Y. Lin, Recyclable enzyme mimic of cubic Fe_3O_4 nanoparticles loaded on graphene oxide-dispersed carbon nanotubes with enhanced peroxidase-like catalysis and electrocatalysis, *J. Mater. Chem. B*, 2014, **2**(28), 4442–4448.

34 J. Yao, K. Zhang, W. Wang, X. Zuo, Q. Yang, H. Tang, M. Wu and G. Li, Remarkable Enhancement in the Photoelectric Performance of Uniform Flower-like Mesoporous Fe_3O_4 Wrapped in Nitrogen-Doped Graphene Networks, *ACS Appl. Mater. Interfaces*, 2018, **10**(23), 19564–19572.

35 X. Tong, S. Chen, C. Guo, X. Xia and X. Y. Guo, Mesoporous $NiCo_2O_4$ Nanoplates on Three-Dimensional Graphene Foam as an Efficient Electrocatalyst for the Oxygen Reduction Reaction, *ACS Appl. Mater. Interfaces*, 2016, **8**(42), 28274–28282.

36 R. K. Pandey, Y. Kawabata, S. Teraji, T. Norisuye, Q. Tran-Cong-Miyata, S. Soh and H. Nakanishi, Metal Nanowire-Based Hybrid Electrodes Exhibiting High Charge/Discharge Rates and Long-Lived Electrocatalysis, *ACS Appl. Mater. Interfaces*, 2017, **9**(41), 36350–36357.

37 Y. Shen, Y. Zhang, X. Zhang, X. Zhou, X. Teng, M. Yan and H. Bi, Horseradish peroxidase-immobilized magnetic mesoporous silica nanoparticles as a potential candidate to eliminate intracellular reactive oxygen species, *Nanoscale*, 2015, **7**(7), 2941–2950.

38 J. Yao, K. Zhang, W. Wang, X. Zuo, Q. Yang, H. Tang, M. Wu and G. Li, Functional integration and self-template synthesis of hollow core-shell carbon mesoporous spheres/Fe_3O_4/nitrogen-doped graphene to enhance catalytic activity in DSSCs, *Nanoscale*, 2018, **10**(17), 7946–7956.

39 C. Cao, L. Wei, G. Wang and J. Shen, Superiority of boron, nitrogen and iron ternary doped carbonized graphene oxide-based catalysts for oxygen reduction in microbial fuel cells, *Nanoscale*, 2017, **9**(10), 3537–3546.

40 X. Sun, D. Li, S. Guo, W. Zhu and S. Sun, Controlling core/shell Au/FePt nanoparticle electrocatalysis *via* changing the core size and shell thickness, *Nanoscale*, 2016, **8**(5), 2626–2631.

41 L. Zhuang, W. Zhang, Y. Zhao, H. Shen, H. Lin and J. Liang, Preparation and characterization of Fe_3O_4 particles with novel nanosheets morphology and magnetochromatic property by a modified solvothermal method, *Sci. Rep.*, 2015, **5**, 9320.

42 T. Wang, P. Xiao, L. Ye, P. Zhu and L. Zhuang, Coupling Au-loaded magnetic frameworks to photonic crystal for the improvement of photothermal heating effect in SERS, *RSC Adv.*, 2023, **13**(8), 5002–5012.

43 C. Wang, J. Wang, P. Li, Z. Rong, X. Jia, Q. Ma, R. Xiao and S. Wang, Sonochemical synthesis of highly branched flower-like Fe_3O_4@SiO_2@Ag microcomposites and their application as versatile SERS substrates, *Nanoscale*, 2016, **8**(47), 19816–19828.

44 X. Ren, T. Wu, Y. Sun, Y. Li, G. Xian, X. Liu, C. Shen, J. Gracia, H. J. Gao, H. Yang and Z. J. Xu, Spin-polarized oxygen evolution reaction under magnetic field, *Nat. Commun.*, 2021, **12**(1), 2608.

45 F. A. Garcés-Pineda, M. Blasco-Ahicart, D. Nieto-Castro, N. López and J. R. Galán-Mascarós, Direct magnetic enhancement of electrocatalytic water oxidation in alkaline media, *Nat. Energy*, 2019, **4**(6), 519–525.

46 L. Cai, J. Huo, P. Zou, G. Li, J. Liu, W. Xu, M. Gao, S. Zhang and J. Q. Wang, Key Role of Lorentz Excitation in the Electromagnetic-Enhanced Hydrogen Evolution Reaction, *ACS Appl. Mater. Interfaces*, 2022, **14**(13), 15243–15249.

47 X. Liu, P. Zou, L. Song, B. Zang, B. Yao, W. Xu, F. Li, J. Schroers, J. Huo and J.-Q. Wang, Combinatorial High-Throughput Methods for Designing Hydrogen Evolution Reaction Catalysts, *ACS Catal.*, 2022, **12**(7), 3789–3796.

48 T. Wu, X. Ren, Y. Sun, S. Sun, G. Xian, G. G. Scherer, A. C. Fisher, D. Mandler, J. W. Ager, A. Grimaud, J. Wang, C. Shen, H. Yang, J. Gracia, H. J. Gao and Z. J. Xu, Spin pinning effect to reconstructed oxyhydroxide layer on ferromagnetic oxides for enhanced water oxidation, *Nat. Commun.*, 2021, **12**(1), 3634.

49 J. Barrio, A. Pedersen, S. Favero, H. Luo, M. Wang, S. C. Sarma, J. Feng, L. T. T. Ngoc, S. Kellner, A. Y. Li, A. B. Jorge Sobrido and M. M. Titirici, Bioinspired and Bioderived Aqueous Electrocatalysis, *Chem. Rev.*, 2023, **123**(5), 2311–2348.

50 H. Chen, O. Simoska, K. Lim, M. Grattieri, M. Yuan, F. Dong, Y. S. Lee, K. Beaver, S. Weliwatte, E. M. Gaffney and S. D. Minteer, Fundamentals, Applications, and Future Directions of Bioelectrocatalysis, *Chem. Rev.*, 2020, **120**(23), 12903–12993.

51 C. Santoro, P. Bollella, B. Erable, P. Atanassov and D. Pant, Oxygen reduction reaction electrocatalysis in neutral media for bioelectrochemical systems, *Nat. Catal.*, 2022, **5**(6), 473–484.

52 A. Ruff, F. Conzuelo and W. Schuhmann, Bioelectrocatalysis as the basis for the design of enzyme-based biofuel cells and semi-artificial biophotoelectrodes, *Nat. Catal.*, 2019, **3**(3), 214–224.

53 H. Chen, F. Dong and S. D. Minteer, The progress and outlook of bioelectrocatalysis for the production of chemicals, fuels and materials, *Nat. Catal.*, 2020, **3**(3), 225–244.